

Exploring dust formation in the episodic WCd system WR140

J. W. Eatson^{*} & J. M. Pittard

School of Physics and Astronomy, University of Leeds, Woodhouse Lane, Leeds LS2 9JT, UK

Accepted XXX. Received YYY; in original form ZZZ

ABSTRACT

Key words: stars: Wolf-Rayet – methods: numerical – binaries: general

1 INTRODUCTION

The dynamics of massive stars in binary systems is a particularly fascinating subject. These incredibly violent systems are obscured behind vast clouds of outflowing stellar wind, the result of the most massive stars we know of slowly tearing themselves asunder. Colliding Wind Binary (CWB) systems were first hypothesised as an explanation of the source of highly luminous and variable x-ray sources such as V444 Cyg and γ^2 Vel (Prilutskii & Usov 1976). These extremely bright emissions were due to stellar wind collision with shock velocities in the order of 10^3 km s^{-1} . The variability in x-ray emission is easily explained in the case of a binary system due to a number of factors, such as the Wind Collision Region (WCR) being occluded by the outflowing stellar wind, being occluded by the stars themselves, or the system can have an eccentric orbit, reducing the shock strength as the orbital separation, d_{sep} , changes. Despite this dust-hostile environment, CWB systems containing a Wolf-Rayet carbon phase star (WC) have been observed producing copious quantities of dust (so-called WCd systems). These systems, where the WC star is typically paired with a main sequence OB star, typically convert around 1% of the stellar wind into dust a short time after wind collision. In more prolific systems such as WR104, however, the dust-to-gas mass fraction, z , of the system can be as high as 36% (Lau et al. 2020). This corresponds to dust production rates on the order of $10^{-6} M_{\odot} \text{ yr}^{-1}$, rivalling other profuse dust producing phenomena such as AGB stars.

WCd systems can sub-categorised further, into persistent, variable and episodic dust forming systems. Persistent systems, such as WR104 (Tuthill et al. 1999), produce dust at a constant rate, and as such produce extreme quantities of dust, as well as well-defined pinwheel patterns if the system is viewed face-on. Episodic systems, meanwhile, only produce dust for a limited period, before entering a period of dormancy; this pattern is cyclical, and is predictably periodic. A good example of such an episodic system is WR140, the subject of this paper (Williams et al. 1990). Variable systems have some characteristics of these two sub-types, having a distinct variability without a period of dust producing dormancy, such as WR98a (Monnier et al. 1999). Whether a system is persistent, variable or episodic is based on the systems orbital eccentricity, highly eccentric

systems appear to form episodic systems, with the “active” dust production period occurring immediately after periastron passage, and a relatively short time thereafter. Meanwhile, persistent and variable systems have been observed to have more circular orbits, suggesting that the effect of a change in system separation distance, d_{sep} , has a role in dust formation. The initial mechanism behind dust formation is not well understood, whilst nascent amorphous carbon dust grain cores can form condense within the photosphere of WC7-9 stars, these grain cores would be vaporised by UV flux of both stars. However, within the WCR these grains appear to flourish, observations of these systems show that infrared excess in wavelengths associated with amorphous grains is detected almost exclusively within the post-shock WCR (Soulain et al. 2018). Observations also indicate that dust formation occurs rapidly and close to the system, this requires strong radiative cooling for the immediate-post shock temperature to reduce from $\sim 10^8 \text{ K}$ to $\sim 10^4 \text{ K}$ (Williams et al. 1987, 1990). As such, dust formation appears to be encouraged in the WCR through a multitude of factors:

- The high density of the post-shock WCR results in a high collision rate between carbon atoms and dust grains.
- The WCR shields nascent dust grains from the bulk of the UV emission from the stars.
- The rapid cooling in the immediate post-shock environment reduces gas-grain sputtering.
- Strong radiative cooling drives the formation of thermal instabilities, which produces clumps of cool, high density gas where dust can rapidly grow.

This dust formation can also be influenced by orbital separation, velocity shear and momentum ratio imbalance between the winds, producing variability.

WCd systems are comparatively rare, out of 106 confirmed systems with a WR binary, only 9 are found to be categorised as episodic WCd systems (Table 1). This makes observation of these systems difficulty, as these systems have a typical distance on the order of 1 – 10 kpc. Whilst these systems can be observed and the dusty WCR can be resolved, observation of the innermost, immediate post-shock dust forming region is not possible at this distance. As such, numerical simulation is necessary to determine dust formation in WCd systems, a contemporary example of such simulations is Hendrix et al. (2016), though simulation of the evolution of dust grains, through cooling, growth and sputtering was not performed. In this paper we

^{*} E-mail: py13je@leeds.ac.uk

	Persistent		Variable		Episodic	
	Total	Example	Total	Example	Total	Example
WC4	1	WR19	0	—	0	—
WC5	0	—	0	—	1	WR47C
WC6	1	WR124-10	0	—	0	—
WC7	3	WR102-22	0	—	4	WR140
WC8	6	WR13	1	WR48a	3	WR122-14
WC9	45	WR104	6	WR98a	1	WR75-11
Total	56		7		9	

Table 1. Number of confirmed WCd systems with known spectral type and dust formation type from the Galactic Wolf Rayet Catalogue (Rosslowe & Crowther 2015). Systems with uncertain spectral types not included, while systems labelled “d” are included within the “persistent” category for their associated spectral type.

present a numerical simulation of the archetypical episodic WCd system WR140 with a co-moving dust model simulating grain growth and sputtering through gas-grain collisions. This simulation covers a temporal slice of the orbit of WR140 from phase $\Phi = 0.95$ to $\Phi = 1.10$, or the period immediately prior to and after periastron passage. We will discuss our methodology in Section 2, with a particular emphasis on our dust model in Subsection 2.2. Afterwards we will discuss the simulation and WR140 system parameters, as well as our data collection techniques in Section 3. Finally, we will discuss our results and conclude in Sections 4 and 5.

2 METHODOLOGY

The periodic dust forming system WR140 was simulated using a fork of the Athena++ hydrodynamical code (Stone et al. 2020), a series of modifications were implemented to simulate binary system orbits, stellar wind outflows and dust evolution. These simulations were conducted in 3D in a Cartesian co-ordinate system. The code solves a Riemann problem at each cell interface to determine the time-averaged values at the zone interfaces, and then solves the equations of hydrodynamics:

$$\frac{\partial \rho}{\partial t} + \nabla \cdot (\rho \mathbf{u}) = 0, \quad (1a)$$

$$\frac{\partial \rho \mathbf{u}}{\partial t} + \nabla \cdot (\rho \mathbf{u} \mathbf{u} + P) = 0, \quad (1b)$$

$$\frac{\partial \rho \varepsilon}{\partial t} + \nabla \cdot [\mathbf{u} (\rho \varepsilon + P)] = \dot{E}_{\text{cool}}, \quad (1c)$$

where ε is the total specific energy ($\varepsilon = \mathbf{u}^2/2 + e/\rho$), ρ is the gas density, e is the internal energy density, P is the gas pressure and \mathbf{u} is the gas velocity. In order to simulate radiative losses, the parameter \dot{E}_{cool} is included, which is the energy loss rate per unit volume from the fluid due to gas and dust cooling. Spatial reconstruction using a piecewise linear method was performed, while two strong stability Runge-Kutta methods were used for numerical integration, depending on the simulation stability. Several passive scalars are utilised to model wind mixing and dust evolution, the scalar values are transported by the fluid, for a given scalar species i , the scalar is advected through the scalar through the following equation:

$$\rho \frac{dC_i}{dt} = \frac{\partial}{\partial t} (\rho C_i) + \nabla \cdot (C_i \rho \mathbf{u}) = -\nabla \cdot \mathbf{Q}_i, \quad (2)$$

where $\mathbf{Q}_i = -\nu_{ps} \rho \nabla C_i$ is the diffusive flux density and ν is the passive scalar diffusion coefficient (Stone et al. 2020).

Stellar winds are simulated by modifying the density, ρ_R , momentum, p_R , and energy, E_R in a small region around both stars. Winds flow from this “remap” region at the stars wind terminal velocity, v^∞ . Remap zone parameters are calculated with the formulae

$$\rho_R = \frac{\dot{M}}{4\pi r^2 v_\infty}, \quad (3a)$$

$$p_R = \rho_R v_r, \quad (3b)$$

$$E_R = \frac{P_R}{\gamma - 1} + \frac{1}{2} \rho_R v_\infty^2, \quad (3c)$$

where P_R is the cell pressure, $P_R = \rho_R k_B T_w / \mu m_H$, T_w is the wind temperature, μ is the mean molecular mass, m_H is the mass of a hydrogen atom, v_R is the wind velocity as it flows radially from the center of the “remap zone” and r is the distance from the current cell to the centre of the remap zone. This method produces radially out-flowing winds from the star with an expected density and velocity. This method is stable against numerical instability, while also allowing us to precisely control the winds.

Line driving and wind acceleration effects are not simulated, which can result in divergence with the correct wind velocity as stars approach periastron passage. Instead, winds are instantaneously accelerated to their terminal velocity. Additionally, influence from either gravitational self-interaction and interaction with the stars gravity wells is not simulated, with the stellar winds assumed to be travelling far in excess of the system escape velocity.

Athena++ utilises Message Passing Interface (MPI) parallelism. The numerical problem is broken into blocks, which are distributed between processing nodes on a High Performance Compute (HPC) cluster. The block size is variable, but for these simulations a block size of $40 \times 40 \times 10$ cells in XYZ was found to be optimal. Adaptive Mesh Refinement was considered for this simulation, however a known issue with the Athena++ code prevented this from being possible. Passive scalars incorporated into the simulation were found to not be conserved along the interfaces between mesh blocks undergoing refinement, this meant that the simulation would behave non-physically (This bug is recorded as issue #365 on the Athena++ Github repository¹). A ring of refined cells across the orbital path was considered, but the performance improvements of this method were found to be negligible and not worth pursuing, as the block based refinement method of Athena++ would result in much redundant refinement. Instead, a static mesh is used, where the stars predicted orbit over the simulation is refined to the maximum level, with a gradual de-refinement away from this refinement region.

2.1 Radiative cooling

Cooling is simulated via the removal of energy from a cell at each time-step. A cooling rate, dE/dt , is calculated, and integrated using a sub-stepping Euler method, with the number of sub-steps determined by the estimated cooling timescale of the cell. Cooling due to gas and plasma emission in the stellar winds are calculated via individual lookup tables from each wind. These lookup tables contain the normalised emissivity, $\Lambda_w(T)$ for a specific temperature from 10^4 to 10^9 K. The cooling rate is determined for a cell by calculating the cell temperature, and estimating $\Lambda_w(T)$ using linear interpolation between the nearest emissivity values in the lookup table. The energy loss is then calculated through the equation

¹ <https://github.com/PrincetonUniversity/athena/issues/365>

$$\frac{dE}{dt} = \left(\frac{\rho}{m_H} \right)^2 \Lambda_w(T), \quad (4)$$

where ρ is the gas density and m_H is the mass of hydrogen. The lookup table was generated by mixing a series of cooling curves from MEKAL simulations of elemental gasses. These curves were combined based on the elemental abundances in the WC and OB winds. To save calculation time, temperatures between $1 \times 10^4 \text{ K} < T \leq 1.1 \times 10^4 \text{ K}$ are set to $1 \times 10^4 \text{ K}$ as they are assumed to be either rapidly cooling or a part of the stellar wind outside of the WCR.

2.2 Dust model

In order to simulate dust evolution in WR140, included in the hydrodynamical code is a passive scalar dust model that simulates dust growth through collisions between dust grains and carbon atoms, and destruction through sputtering from a hot wind. The dust model operates on passive scalars, and as such simulates dust that is co-moving with the stellar wind. Two scalars are used to describe dust in a cell, a , the grain radius in μm , and z , the grain dust-to-gas mass ratio:

$$z = \frac{\rho_d}{\rho_g}, \quad (5)$$

where ρ_d is the dust density in a cell and ρ_g is the gas density in a cell. A number of assumptions are made in this dust model, for instance, the dust grains in the model are spherical, with a uniform density. Furthermore, dust grains are assumed to have a single size in a region, as well as a constant number density. As such, this model does not simulate grain agglomeration and fracturing. Additional mechanisms for dust formation and destruction could also be implemented such as grain-grain agglomeration and photoevaporation. A multi-fluid model with drag force coupling could also be implemented, however this is beyond the scope of this paper.

Dust is grown through grain accretion using formulae described by (Spitzer 2008) where dust grains grow via low-velocity collisions with surrounding carbon atoms, causing them to accrete onto the surface of the dust grain. Carbon is removed from the gas, reducing the cell density, while the corresponding dust density increases. This ensures that mass is preserved in the simulation. Assuming a single average grain size the rate of change in the grain radius in a cell, da/dt , is given by the equation:

$$\frac{da}{dt} = \frac{\xi \rho_C w_C}{4 \rho_{gr}}, \quad (6)$$

where ξ is the grain sticking factor, ρ_C is the carbon density ($\rho_C = X_C \rho_g$), w_C is the Maxwell-Boltzmann RMS velocity for carbon ($w_C = \sqrt{3k_B T / 12m_H}$), k_B is the Boltzmann constant and ρ_{gr} is the grain bulk density. The rate of change in grain mass due to accretion, $dm_{gr,ac}/dt$, is calculated with the formulae:

$$\frac{dm_{gr,ac}}{dt} = 4\pi \rho_{gr} a^2 \frac{da}{dt} = \pi \xi \rho_C w_C a^2, \quad (7)$$

A bulk density approximating that of amorphous carbon grains ($\rho_{gr} = 3.0 \text{ g cm}^{-3}$) is used for this simulation.

Dust destruction gas-grain sputtering is calculated using the Draine & Salpeter (1979) prescription. Within a flow of number density n_g a dust grain of radius a has a grain lifespan, τ_{gr} of:

$$\tau_{gr} = \frac{a}{\dot{a}} \approx 3 \times 10^6 \frac{a}{n_g} \text{ yr}. \quad (8)$$

This value is based on an average lifetime of carbon grains in an interstellar shock with a temperature of $1 \times 10^6 \text{ K} \leq T \leq 3 \times 10^8 \text{ K}$ (Tielens et al. 1994; Dwek et al. 1996). The rate of change in the dust grain mass due to sputtering, $dm_{gr,sp}/dt$, can then be calculated with a similar formulae to the rate of change in grain mass due to accretion:

$$\frac{dm_{gr,sp}}{dt} = 4\pi \rho_{gr} a^2 \frac{da}{dt} = -4\pi \tau_{gr} n_g a^2. \quad (9)$$

Finally, the total rate of change in grain mass is calculated, the overall change in dust density is then calculated:

$$\frac{d\rho_d}{dt} = \left(\frac{dm_{gr,acc}}{dt} + \frac{dm_{gr,sp}}{dt} \right) n_d, \quad (10)$$

where n_d is the dust grain number density.

Cooling via emission of photons from dust grains is also included in this model. The rate of cooling is calculated using the uncharged grain case of the prescription described in (Dwek & Werner 1981). Grains are collisionally excited by collisions with ions and electrons, causing them to radiate. Similarly to the gas/plasma emission model used, the emitted photons are not re-adsorbed by the WCR medium, causing energy to be removed from the simulation. This therefore makes the assumption that the WCR is optically thin to far-infrared photons, which is observationally correct. The grain heating rate (in erg s^{-1}) for a dust grain is calculated with the formulae:

$$H = 1.26 \times 10^{-19} \frac{n_g}{A^{1/2}} a^2 (\mu\text{m}) T^{3/2} h(a, T), \quad (11)$$

where H is the heating rate due to atom and ion collisions, n is the particle number density, A is the mass of the incident particle in AMU, $a(\mu\text{m})$ is the grain radius in microns, T is the temperature of the ambient gas, and $h(a, T)$ is the effective grain heating factor. Individual heating rates for hydrogen, helium, carbon, nitrogen and oxygen are calculated, in order to calculate the total ion collisional heating, H_{coll} :

$$H_{\text{coll}} = H_H + H_{\text{He}} + H_C + H_N + H_O. \quad (12)$$

The effective grain heating factor for each element is calculated via the equation:

$$h(a, T) = 1 - \left(1 + \frac{E^*}{2k_B T} \right) e^{-E^*/k_B T}, \quad (13)$$

where E^* is the critical energy required to overcome the grain's potential (Table 2). The rate of heating due to electron-grain collisions, H_{e1} , is similar to Eq. 11. The grain heating factor for electron collisions, h_e , is calculated via an approximation from Dwek & Werner (1981). This approximation is performed as a complex integration for every cell and cooling step would need to be performed instead, which was found to take up $> 90\%$ of the processing time for a cell. h_e is estimated through the following conditions:

$$\begin{aligned} h_e(x^*) &= 1, & x^* &> 4.5, \\ &= 0.37x^{*0.62}, & x^* &> 1.5, \\ &= 0.27x^{*1.50}, & \text{otherwise,} \end{aligned} \quad (14)$$

where $x^* = 2.71 \times 10^8 a^{2/3} (\mu\text{m}) / T$. This approximation differs from the integration method by less than 8% while being 4 orders of

Particle	E^*
e^-	$23 a^{2/3} (\mu\text{m})$
H	$133 a (\mu\text{m})$
He	$222 a (\mu\text{m})$
C	$665 a (\mu\text{m})$
N	$665 a (\mu\text{m})$
O	$665 a (\mu\text{m})$

Table 2. Grain potential critical energy, E^* , for a dust grain of a in μm for electrons, e^- , as well as the elements considered for grain cooling. The values for carbon, oxygen and nitrogen are identical.

magnitude faster. Excitation due to grain-grain collisions were not modelled, due to the limitations of the passive scalar model. In order to calculate the change in energy due to dust cooling, we find the radiative emissivity for dust, $\Lambda_d(T, a)$, to be

$$\Lambda(T, a) = \frac{H_{\text{coll}} + H_{\text{el}}}{n_{\text{H}}}, \quad (15)$$

where n_{H} is the number density of hydrogen in the gas. The energy loss rate from dust cooling, dE_d/dt , then calculated with the equation:

$$\frac{dE_d}{dt} = n_{\text{T}} n_d \Lambda_d(T, a), \quad (16)$$

and summated with the gas/plasma energy loss rate.

3 SYSTEM PARAMETERS

The authors of this paper have previously simulated WCd systems in the form of a parameter space exploration, in order to discern which wind and orbital parameters influence the dust formation rates of a typical WCd system. It was determined that the primary factors of dust formation in a WCd system were the mass loss rates, \dot{M} , and wind terminal velocities, v^∞ , for each star, as well as the orbital separation, d_{sep} . In particular, it was found that imbalances between the wind velocity was found to produce a shear effect, driving the formation of Kelvin-Helmholtz instabilities. Slower winds were found to be more radiative in the post-shock WCR, cooling down to temperatures adequate for dust formation, this was found to influence the dust formation rate by as much as six orders of magnitude by varying the WR wind terminal velocity by a factor of 4. The authors also found that increasing d_{sep} significantly reduced the dust production rate, due to less intensive shocks as the out-flowing winds became thinner with distance. In the case of WCd systems with eccentric orbits, the separation distance can vary significantly, in the case of WR140 d_{sep} varies by a factor of 18 from apastron to periastron, this is hypothesised to be the primary cause of dust production variability within episodic systems. As \dot{M} does not vary significantly on the orbital timescale of these systems, this is not expected to impact the dust formation rate in episodic systems, while the wind velocity can diverge somewhat due to radiative inhibition and orbital motion, which was considered in our results.

In order to understand the structure and dynamics of the CWB system we must define some important parameters. The wind momentum ratio, η , is defined as:

$$\eta = \frac{\dot{M}_{\text{OB}} v_{\text{OB}}^\infty}{\dot{M}_{\text{WR}} v_{\text{WR}}^\infty}, \quad (17)$$

as η decreases we find that the wind becomes more imbalanced, in

the case of WR+OB CWB systems we find that the WR stars wind typically dominates the system. Assuming that there is no radiative inhibition (Stevens & Pollock 1994) or radiative braking (Gayley et al. 1997), we can approximate the WCR to a conical region with an opening angle:

$$\theta_c \simeq 2.1 \left(1 - \frac{\eta^{2/5}}{4} \right) \eta^{-1/3} \quad \text{for } 10^{-4} \leq \eta \leq 1, \quad (18)$$

to a relatively high degree of accuracy (Eichler & Usov 1993). Another important value for determining the evolution of a CWB system is the cooling parameter, χ , which is the ratio of the time taken for the shocked wind to completely cool to the time taken for the wind to escape the shock region:

$$\chi = \frac{t_{\text{cool}}}{t_{\text{esc}}} \approx \frac{v_8^4 d_{12}}{\dot{M}_{-7}}, \quad (19)$$

where v_8 is the wind terminal velocity in units of 10^8 cm s^{-1} , d_{12} is the separation distance in units of 10^{12} cm and \dot{M}_{-7} is the wind mass loss rate in units of $10^{-7} M_\odot \text{ yr}^{-1}$ (Stevens et al. 1992). As $\chi \rightarrow 1$, the structure of the WCR becomes more influenced by radiative instabilities, and has a post-shock temperature approaching the initial wind temperature. If $\chi < 1$, the WCR is completely dominated by instabilities, while if $\chi \gg 1$, the system behaves adiabatically. If the WCR is highly radiative the post-shock compression can be significantly greater than the adiabatic limit of $\rho_{\text{post-shock}} = 4\rho_{\text{pre-shock}}$, which as previously discussed facilitates higher rates of dust production. Finally, we define a maximum dust production rate from the system, $\dot{M}_{\text{d,max}}$, assuming a 100% conversion rate of WR wind in the WCR into dust. The fraction of the WR wind that is passed through the WCR is given by the equation:

$$f_{\text{WR}} = \frac{1 - \cos(\theta_{\text{WR}})}{2}, \quad (20)$$

where θ_{WR} is the opening angle of the WR shock front ($\theta_{\text{WR}} \approx 2 \tan^{-1}(\eta^{1/3}) + \pi/9$). $\dot{M}_{\text{d,max}}$ is then calculated with the formulae:

$$\dot{M}_{\text{d,max}} = \dot{M}_{\text{WR}} X_{\text{C,WR}} f_{\text{WR}}, \quad (21)$$

where X_{C} is the carbon mass fraction in the WR star (Pittard & Dawson 2018).

3.1 WR140 parameters

WR 140 was simulated in this paper as it is considered to be the archetypical episodic CWB system, whose infrared dust emission peaks around periastron passage. WR 140 deviates from WR 98a and WR 104 by having an extremely eccentric orbit, which significantly effects the cooling parameter as the orbit progresses. Additionally, the minimum value for χ is significantly larger than the other systems, and hence cooling would be less dominant on the dynamics of the WCR, even at periapsis. Though these simulations do not calculate wind acceleration due to radiative line driving, both stellar winds are expected to be accelerated close to their terminal wind velocities (Lamers & Cassinelli 1999). However, this discrepancy should be noted when considering the results of this paper.

Recent improved estimations of the orbital parameters of WR140 by Thomas et al. (2021) were used to calculate the orbital path for these simulations, while the mass loss rate, \dot{M} , and the wind terminal velocity, v^∞ , were derived from Williams et al. (1990) (Table 3).

Parameter	Value	Citation
M_{WR}	$10.31 M_{\odot}$	Thomas et al. (2021)
M_{OB}	$29.27 M_{\odot}$	Thomas et al. (2021)
P	7.926 yr	Thomas et al. (2021)
e	0.8993	Thomas et al. (2021)
\dot{M}_{WR}	$5.6 \times 10^{-5} M_{\odot} \text{ yr}^{-1}$	Williams et al. (1990)
\dot{M}_{WR}	$1.6 \times 10^{-6} M_{\odot} \text{ yr}^{-1}$	Williams et al. (1990)
v_{WR}^{∞}	$2.86 \times 10^3 \text{ km s}^{-1}$	Williams et al. (1990)
v_{OB}^{∞}	$3.20 \times 10^3 \text{ km s}^{-1}$	Williams et al. (1990)
η	0.031	Calculated
χ_{\min}	2.69	Calculated

Table 3. WR140 system parameters.

Element	Solar	WC
X_H	0.705	0.000
X_{He}	0.275	0.546
X_C	0.003	0.400
X_N	0.001	0.000
X_O	0.010	0.050

Table 4. Abundances used for the OB and WR stars being simulated. Other elements are assumed trace when calculating dust emission (Williams et al. 2015).

In order to correctly calculate cooling and dust growth, the abundances of hydrogen, helium, and metals, particularly CNO must be included in the simulations parameters. A typical wind composition for WC stars was assumed for the Wolf-Rayet star, while a solar abundance was assumed for the OB star (Table 4). The system orbit was calculated using a Keplerian orbital model with the two stars as point-masses.

3.2 Simulation parameters

A domain of $128 \times 128 \times 16$ AU was used for this simulation, with a coarse (0^{th} level) simulation resolution of $400 \times 400 \times 50$ in the XYZ domain. The simulation has 4 refinement levels, corresponding to an effective resolution of $6400 \times 6400 \times 800$ cells and a cell size of 0.02^3 AU. At periastron passage this results in a spacing of ~ 80 cells between the stars, which was found to be enough to adequately resolve the WCR. This simulation has an XY to Z aspect ratio of 8:1 in order to reduce processing time, as the bulk of dust formation was expected to occur a short distance from the WCR. Due to computing limitations, a complete orbit could not be completed without AMR, instead, a section of the systems orbit, corresponding to an orbital phase of $0.95 \leq \Phi \leq 1.10$ was simulated, where Φ is the orbital phase. This section represents the period prior to periastron passage, as well as a brief period after periastron (Fig. 1). This represents a period of approximately 1.2 years of the systems orbit, and the period where much of the dust forms (Crowther 2003). Fig. 2 shows the orbital path overlaid onto the statically refined numerical grid, the area of maximum refinement is around the orbital paths of the stars from $0.94 \leq \Phi \leq 1.11$, in order to ensure that the stars are maximally refined. If the stars leave the regions that are refined to either the 3^{rd} or 4^{th} level unphysical behaviour with regards to wind mapping and dust formation occur, as such the simulation is halted when $\Phi = 1.10$. The simulation was run with two different numerical integrators, a 3^{rd} order accurate Runge-Kutta integrator, `rk3`, and a 4^{th} order accurate, 5-stage, 3 storage register strong stability preserving Runge-Kutta integrator, `ssprk5_4` (Ruuth & Spiteri 2005). The `ssprk5_4` integrator was found to be approximately 60% slower, but markedly more stable. Prior to periastron passage the `rk3` integrator

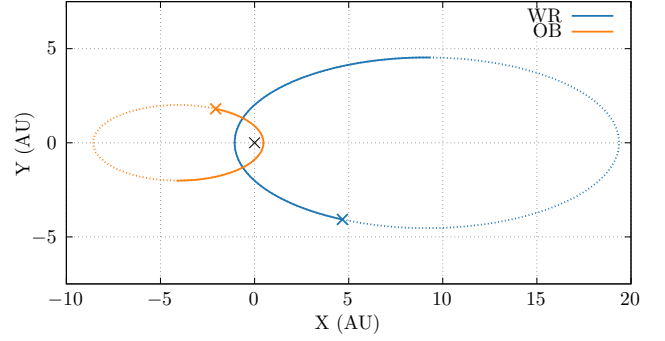


Figure 1. Simulation orbital trajectories of the WC7 and O5 stars in WR140. The solid lines represent the orbital phase being simulated, corresponding to $0.95 \leq \Phi \leq 1.10$, while the dashed lines represent the full orbital trajectory. The starting position for each star and the orbital barycentre at (0,0) have been annotated.

was used for its speed, but increasing numerical instability as the stars grew closer resulted in this proving untenable, and was switched to `ssprk5_4`.

Over periastron passage the average time-step was found to reduce by an order of magnitude, resulting in a corresponding increase to simulation time (Fig. 3). At the most numerically complex portion of the simulation, a Courant number of $C = 0.04$ had to be used instead of the initial value of $C = 0.15$, in order to preserve numerical stability. As the simulation moved past periastron the Courant number was increased every 24 hours of wall time, until C returned to the initial value. The simulation was conducted on the ARC4 HPC cluster at the University of Leeds with 128 cores. The code was compiled using the Intel ICPC compiler using AVX512 optimisations and the Intel MPI library.

3.3 Data collection

Simulation data was exported in the form of HDF5 at regular time intervals - 3D HDF5 meshes were collected every increment of $\Phi = 1.5 \times 10^{-3}$, while 2D slices in the XY plane were collected every increment of $\Phi = 1.5 \times 10^{-4}$. These HDF5 files contain the primitive variables of the simulation: gas density, ρ , gas pressure, P , and wind velocity components, v_x , v_y and v_z . These variables were then used to derive other variables such as temperature and energy. The scalars governing the dust properties were also stored for each cell: the dust-to-gas mass ratio, z , and the dust grain radius, a . The wind “colour”, the proportion of gas from each star, was also tracked. A value of 1.0 indicates a pure WR wind while 0.0 indicates a pure OB wind. The volume-weighted totals of all parameters of interest were also collected, such as the average values for z , a and the dust production rate within the WCR, \dot{M}_d . To calculate \dot{M}_d , a cell must be identified as being within the WCR, this was performed by comparing the cell density to the predicted density of a single wind with the wind parameters of the WC star in the system. Any cell with a density higher a certain threshold value was flagged as being within the WCR. the single-wind density was calculated using the equation:

$$\rho_{SW} = \frac{\dot{M}_{SW}}{4\pi r^2 v_{SW}^{\infty}}, \quad (22)$$

where r is the distance from the barycentre. This threshold value was

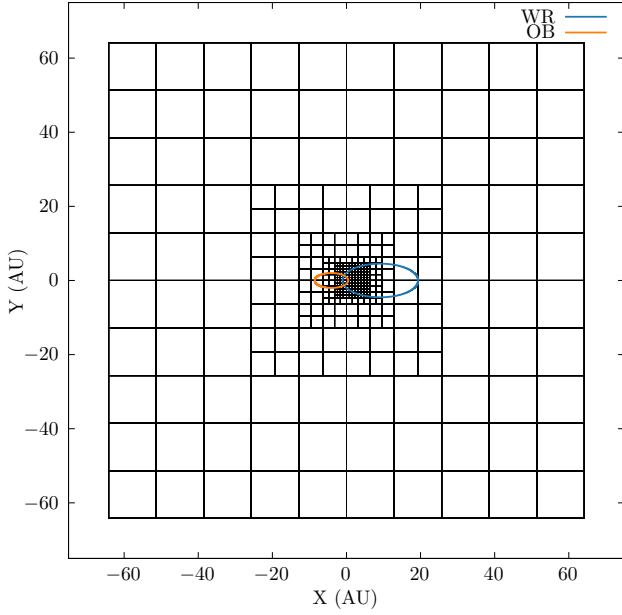


Figure 2. Numerical grid of the WR140 system simulation, static mesh refinement was used to increase the resolution around the orbital path from $0.95 \leq \Phi \leq 1.10$. The orbital path of both stars are overlaid onto this numerical grid. While the stars in the system can be within cells that are not fully refined, if there is insufficient resolution the stars begin to break down. As such the stars are typically in the 3rd or 4th level.

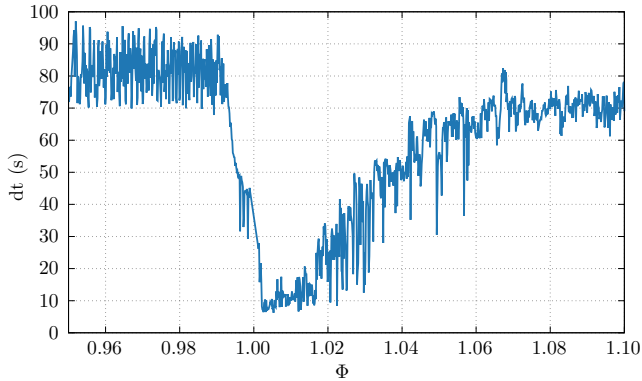


Figure 3. Average timestep, dt , over the course of the WR140 simulation, binned every $\Phi = 0.001$. after periastron passage the `ssprk5_4` numerical integrator and a drastically reduced Courant number was adopted in order to preserve numerical stability. This increased simulation time by approximately an order of magnitude.

set to $\rho_{\text{thres}} = 1.25\rho_{\text{SW}}$, which was found to accurately identify the WCR through prior testing.

4 RESULTS

4.1 Dust yields

The dust production were found to be consistent with the predictions made in our previous paper. After an initial advection period lasting

Parameter	Mean	Maximum	Minimum
\dot{M}_d ($M_\odot \text{ yr}^{-1}$)	7.68×10^{-8}	1.24×10^{-6}	1.30×10^{-19}
\bar{a} (μm)	1.32×10^{-2}	1.44×10^{-2}	5.45×10^{-3}
\bar{z}	3.97×10^{-4}	3.32×10^{-3}	1.60×10^{-7}

Table 5. Advected scalar yields from the WR140 simulation.

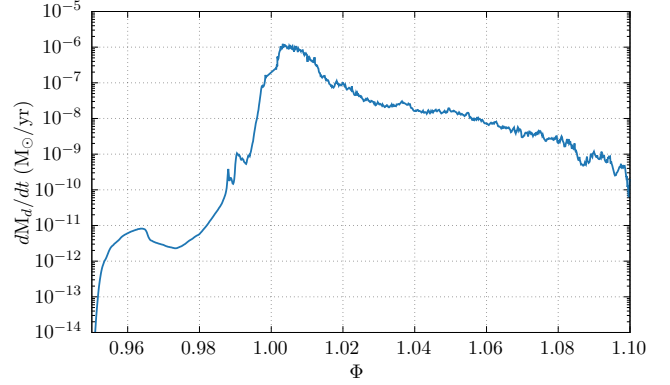


Figure 4.

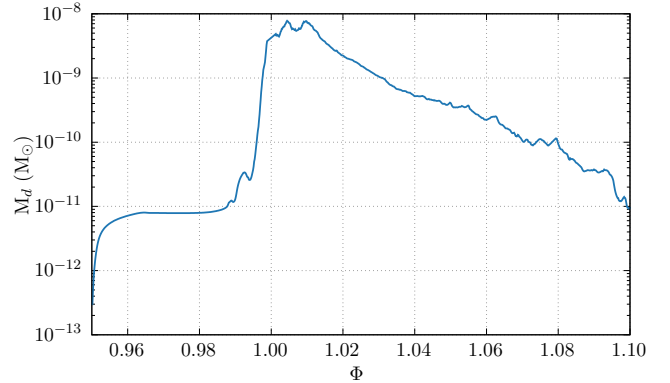


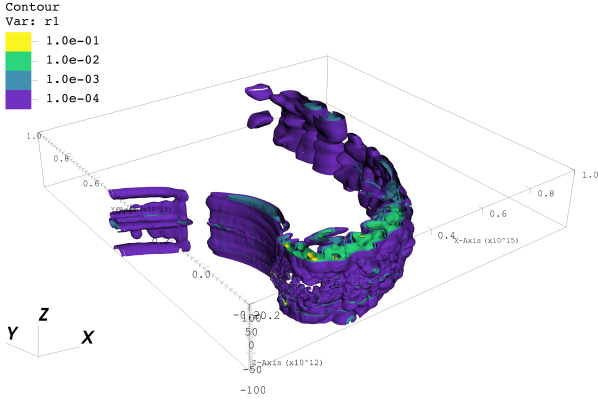
Figure 5.

until $\Phi \approx 0.96$, the dust production rate rapidly increased as the stars approached periastron passage, peaking at $\phi = 1.005$. After this maximum value, the

(Fig. 4)

This is reflected in the overall dust mass of the simulation (Fig. 5), as well as in infrared observations of WR140, where the infrared emission from dust formation rapidly reaches a maximum value after periastron passage, and slowly relaxes to a minimum value. This asymmetry in the time-dependent change in infrared luminosity implies the existence of several factors for suppression and encouragement of dust formation than the change in orbital separation distance.

It should be noted that due to the small size of the simulation, the dust mass in the system will reduce quickly, as dust advects off of the numerical grid.



4.2 Instabilities

4.3 Influence of radial velocity on dust production

4.4 Other changes in velocity shear

5 CONCLUSION

6 ACKNOWLEDGEMENTS

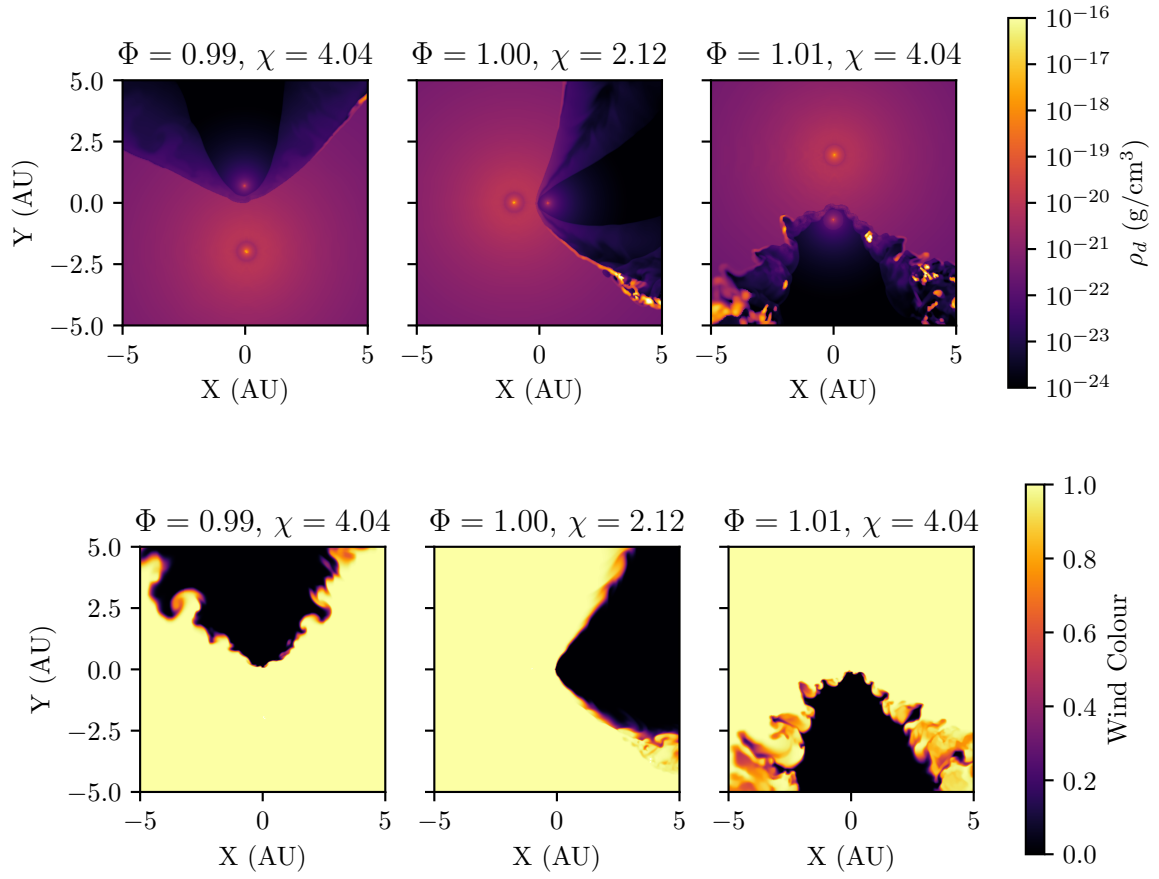
This work was undertaken on ARC4, part of the High Performance Computing facilities at the University of Leeds, UK. We would also like to thank P. A. Crowther for his work on the Galactic Wolf-Rayet Catalogue (pacrowther.staff.shef.ac.uk/WRcat).

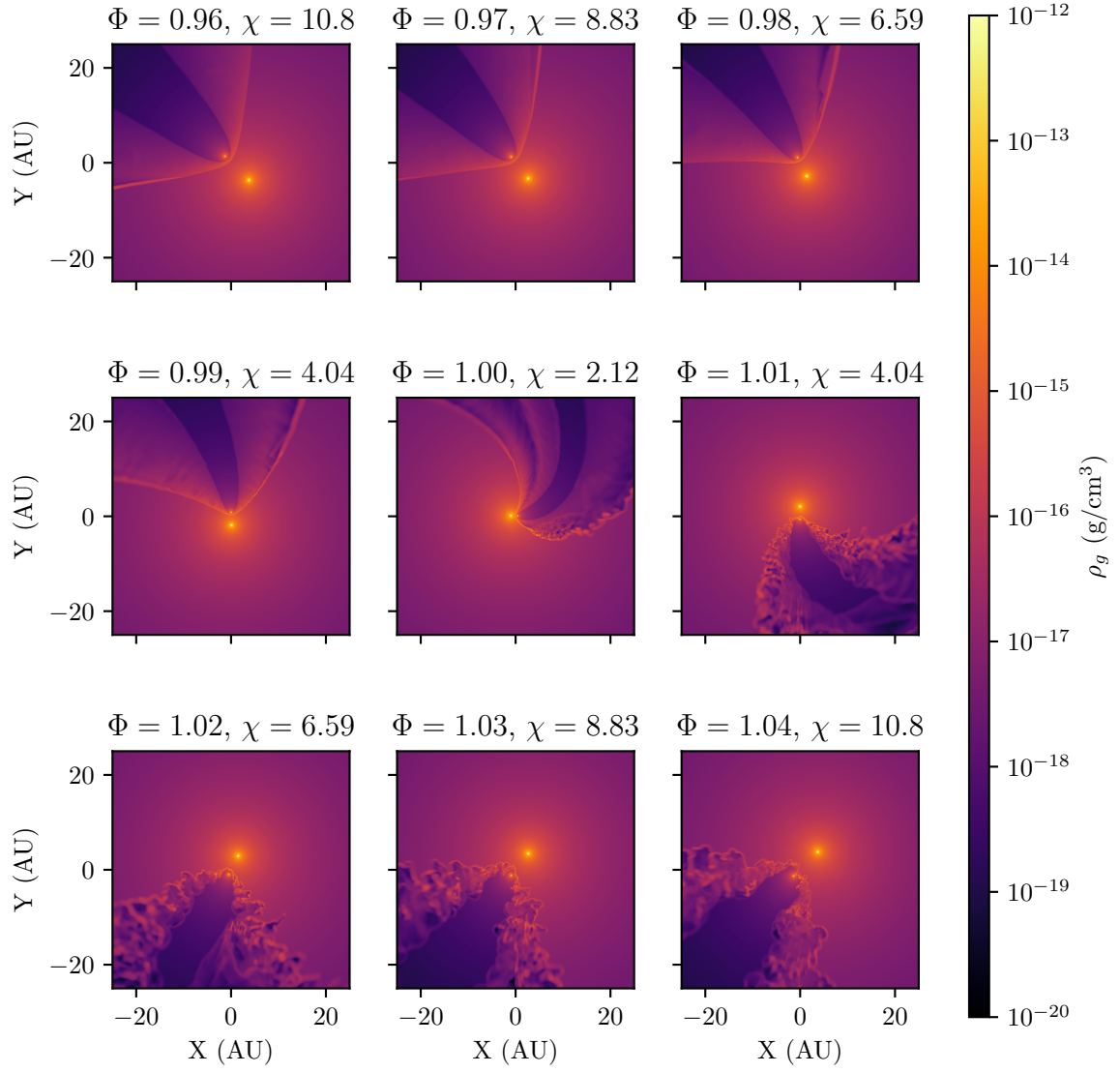
REFERENCES

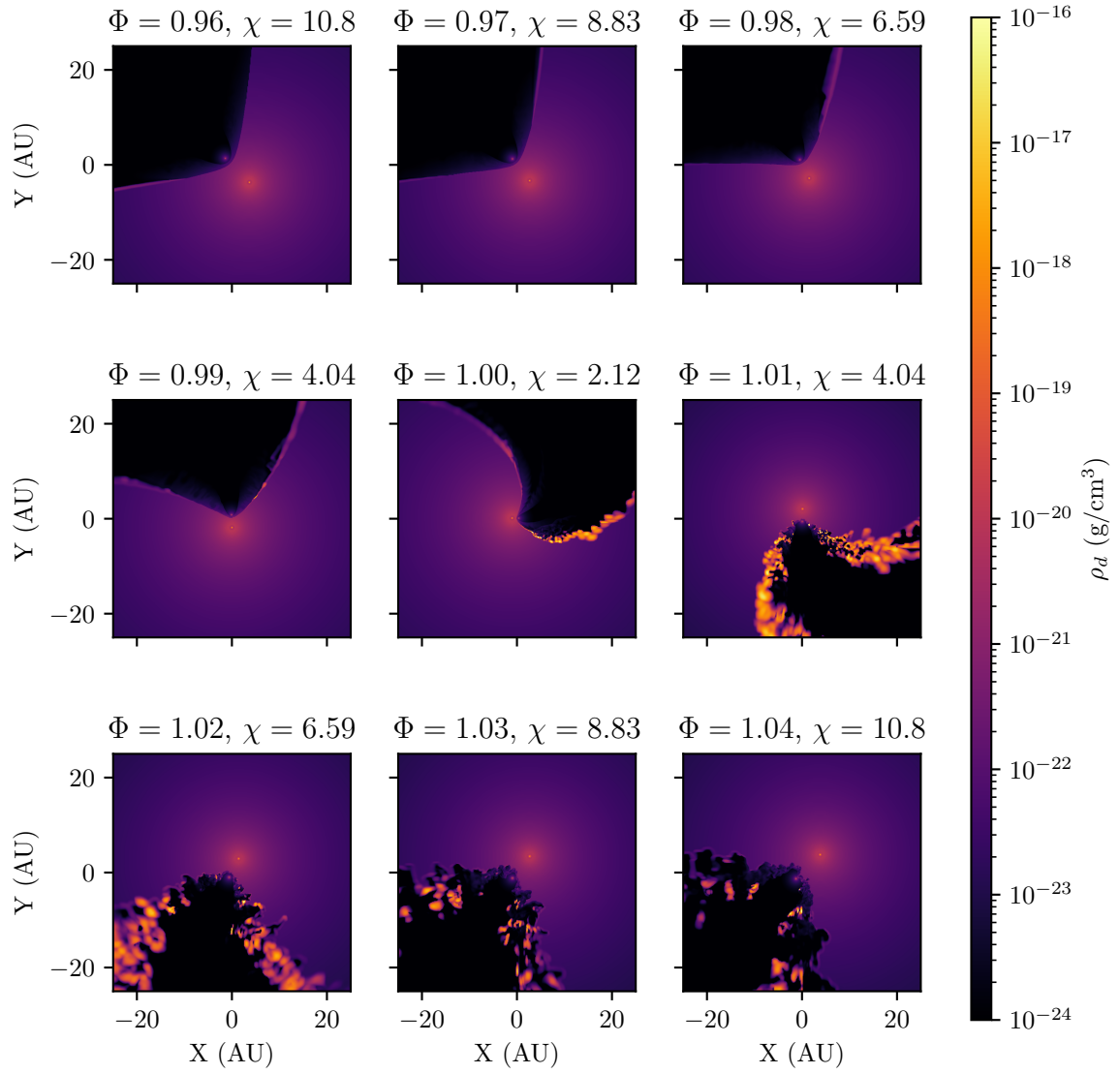
- Crowther P. A., 2003, *Astrophysics and Space Science*, 285, 677
 Draine B. T., Salpeter E. E., 1979, *The Astrophysical Journal*, 231, 77
 Dwek E., Werner M. W., 1981, *The Astrophysical Journal*, 248, 138
 Dwek E., Foster S. M., Vancura O., 1996, *The Astrophysical Journal*, 457, 244
 Eichler D., Usov V., 1993, *The Astrophysical Journal*, 402, 271
 Gayley K. G., Owocki S. P., Cranmer S. R., 1997, *ApJ*, 475, 786
 Hendrix T., Keppens R., van Marle A. J., Camps P., Baes M., Meliani Z., 2016, *Monthly Notices of the Royal Astronomical Society*, 460, 3975
 Lamers H. J., Cassinelli J. P., 1999, *Introduction to Stellar Winds*. Cambridge University Press
 Lau R. M., Eldridge J. J., Hankins M. J., Lamberts A., Sakon I., Williams P. M., 2020, *ApJ*, 898, 74
 Monnier J. D., Tuthill P. G., Danchi W. C., 1999, *ApJ*, 525, L97
 Pittard J. M., Dawson B., 2018, *Mon Not R Astron Soc*, 477, 5640
 Prilutskii O. F., Usov V. V., 1976, *Soviet Astronomy*, 20, 2
 Rosslowe C. K., Crowther P. A., 2015, *Monthly Notices of the Royal Astronomical Society*, 447, 2322
 Ruuth S. J., Spiteri R. J., 2005, *SIAM Journal on Numerical Analysis*, 42, 974
 Soullain A., et al., 2018, *A&A*, 618, A108
 Spitzer L., 2008, *Physical Processes in the Interstellar Medium*. John Wiley & Sons
 Stevens I. R., Pollock A. M. T., 1994, *Mon Not R Astron Soc*, 269, 226
 Stevens I. R., Blondin J. M., Pollock A. M. T., 1992, *The Astrophysical Journal*, 386, 265
 Stone J. M., Tomida K., White C. J., Felker K. G., 2020, *ApJS*, 249, 4
 Thomas J. D., et al., 2021, *Monthly Notices of the Royal Astronomical Society*, 504, 5221
 Tielens A. G. G. M., McKee C. F., Seab C. G., Hollenbach D. J., 1994, *The Astrophysical Journal*, 431, 321
 Tuthill P. G., Monnier J. D., Danchi W. C., 1999, *Nature*, 398, 487

- Williams P. M., van der Hucht K. A., Thé P. S., 1987, *Astronomy and Astrophysics*, 182, 91
 Williams P. M., van der Hucht K. A., Pollock A. M. T., 1990, *Monthly Notices of the Royal Astronomical Society*, 243, 662
 Williams P. M., Crowther P. A., van der Hucht K. A., 2015, *Monthly Notices of the Royal Astronomical Society*, 449, 1834

This paper has been typeset from a \LaTeX file prepared by the author.







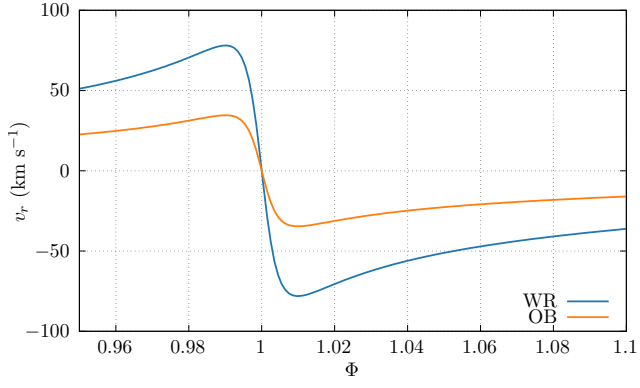


Figure 6. Radial velocity as a function of the orbital phase for the WR and OB stars in the WR140 system relative to the barycentre. As periastron passage occurs, the sudden inversion from approaching to receding can alter the wind velocity of the WR star by as much as 160 km s^{-1} . Whilst this discrepancy is $\sim 6\%$ of the WR wind velocity, this can significantly increase dust production if the stars are receding from each other.